Arch. Metall. Mater. **70** (2025), 2, 539-552

DOI: https://doi.org/10.24425/amm.2025.153454

XIAOLE GE[1,2], I.N. KOLUPAEV[1*], DI JIANG[1,2], HONGFENG WANG[1]

INVESTIGATION OF WELDING FORCES AND TORQUE MEASUREMENT USING OCTAGONAL RING DYNAMOMETER IN REFILL FRICTION STIR SPOT WELDING OF PURE COPPER

The welding forces and torque in refill friction stir spot welding (RFSSW) play a crucial role in optimizing welding process parameters, understanding material deformation and flow mechanisms, improving welding equipment, and analyzing tool wear. To measure the welding forces and torque during pure copper RFSSW, an octagonal ring dynamometer (ORD) was designed and manufactured based on ring deformation theory. A measurement system for welding forces and torque was established, and the ORD was calibrated and validated. Welding experiments were conducted under different process parameters to measure the welding forces and torque during pure copper RFSSW. The variation patterns of welding forces and torque throughout the welding process were analyzed, and the relationships between welding parameters and the peak welding forces and torque were established. The results show that the calibration errors for axial force, torque, and lateral force were 0.97%, 3.78%, and 1.56%, respectively, with cross-sensitivity errors below 5%. The primary welding force during the RFSSW was the axial force, with a peak value more than 10 times that of the lateral force. The clamping, plunging, and refilling stages were the key phases where both welding forces and torque increased significantly. The maximum welding forces occurred near the second dwell stage before the end of welding, while the maximum torque was observed during the plunging stage. Axial force was most influenced by plunge depth, torque was mainly affected by rotational speed, and lateral force was strongly impacted by the combined effects of plunge depth and rotational speed. The average prediction errors for the axial force, torque, and lateral force models were 0.61%, 2.25%, and 1.20%, respectively, with a maximum error of 4.67%. These findings are instrumental in optimizing process parameters to achieve higher weld quality. The study has practical implications for industrial applications, particularly in manufacturing electrical connectors and thin-sheet heat exchangers, where high-quality copper welds are essential. This work also provides a foundation for future research into enhancing the efficiency and reducing the energy consumption of the RFSSW process.

Keywords: RFSSW; copper; welding force; torque; measurement

1. Introduction

Pure copper, known for its excellent electrical and thermal conductivity, is widely used in various fields, including electrical, electronics, energy, and mechanical manufacturing industries [1-4]. When copper sheets are employed as conductive and heat-dissipating structural components, it is often necessary to join different copper sheets to ensure long-term, stable conductive and thermal performance. Welding is a critical method for achieving durable and stable metal joints. However, due to copper's high thermal conductivity and coefficient of expansion, traditional fusion welding methods are not ideal [5,6]. Fortunately, the advent of friction stir spot welding (FSSW) offers a novel approach to achieving high-quality copper welding. FSSW is a solid-state welding process initially developed for joining lightweight metals such as aluminum alloys [7,8]. It has since been expanded for use in joining copper alloys, steel, and other materials [9-11]. The low heat input in FSSW effectively prevents defects such as porosity and hot cracking, commonly encountered in fusion welding [12]. Additionally, the FSSW process does not require filler materials or shielding gas, resulting in low energy consumption. Compared to resistance spot welding, FSSW can save 90% of energy and reduce costs by 40% [13,14]. Currently, three types of FSSW have been extensively studied in public literatures: traditional, sweep, and refill [15]. Traditional FSSW is derived from the principle of friction stir welding (FSW), which includes three stages of plunging, stirring and retracting [16]. In the plunging stage, the tool gradually makes contact with the surface of the workpiece and penetrates to a predetermined depth. The rotation and downward pressure

[1] NATIONAL TECHNICAL UNIVERSITY «KHARKIV POLYTECHNIC INSTITUTE», DEPARTMENT OF MATERIALS SCIENCE, KHARKIV, 61002, UKRAINE
[2] HUANGSHAN UNIVERSITY, COLLEGE OF MECHANICAL AND ELECTRICAL ENGINEERING, HUANGSHAN, 245041, P.R. CHINA

* Corresponding author: igor.kolupaev@gmail.com

of the tool generate frictional heat, softening the material. During the stirring stage, the tool remains at the set depth and continues to rotate, mixing and plastically deforming the softened material through the tool's rotation. After stirring is complete, the tool gradually retracts from the workpiece. At this point, the softened material re-solidifies, forming the weld spot [17-19]. Based on traditional FSSW, the swept FSSW was developed by modifying the tool's motion path [20]. In swept FSSW, the rotating tool first plunges to a specified depth, and then moves a certain distance outward from the weld spot. Subsequently, it follows a circular path, either clockwise or counterclockwise, before finally moving inward to return to the starting point [21-23]. Generally, due to the increased weld area, the joint strength of swept FSSW surpasses that of traditional FSSW [24]. However, the traditional FSSW and swept FSSW leave behind a keyhole defect in the welded area, which, to some extent, weakens the joint strength [25,26]. To eliminate this keyhole defect, the GKSS Research Center in Germany developed a refill friction stir spot welding (RFSSW) process by optimizing tool geometry and tool movement [27,28]. Under appropriate welding processes, RFSSW can complete welding within 1 second without compromising weld quality, making RFSSW an easily implementable welding solution [29]. Compared to traditional FSSW and swept FSSW, RFSSW is preferred for copper welding due to its ability to minimize defects and provide strong joints, which has attracted increasing attention from researchers [30-32].

In RFSSW, the welding forces and torque are key parameters that reflect energy input, material flow, and the interaction between the tool and the workpiece. These parameters significantly influence the quality of weld formation and the reliability and stability of the welding equipment and tooling, as well as the service life of the tool [33,34]. The measurement of welding forces and torque has become a critical consideration for researchers studying RFSSW processes. Some researchers have focused on welding forces and torque in FSSW. Pattanaik et al. explored the feasibility of joining 6061 aluminum alloy and polycarbonate using FSSW. They employed force, torque, velocity, and position sensors to capture variations in force-torque-velocity-displacement signals during the welding process. Their analysis of axial force and torque trends under different process parameters revealed that moderate dwell time, lower plunge depth, or higher rotational speed can reduce axial force, enhance torque, and thus improve weld quality [35]. Andrade et al. measured torque and temperature in FSSW of steel, analyzing the influence of welding parameters on these variables. They developed a predictive model for torque and temperature during welding, finding that tool diameter and rotational speed significantly impact torque and temperature in steel FSSW [36]. Furthermore, Das and Narayanan proposed a novel FSSW using a consumable sheet and applied it to join AA6063-T6 aluminum alloy and CRCA/IS-513 steel. They measured axial force and torque under various welding parameters, discovering that peak axial force and torque occur in the later stages of the plunging stage, while both decrease during the dwell stage. At high rotational speeds, both axial force and torque were lower [37]. Ragab et al. developed a real-time monitoring system for welding force and temperature in FSSW, investigating the effects of tool rotational speed, plunging rate, and dwell time on axial force and peak temperature. They further constructed a model linking welding parameters with axial force and peak temperature [38]. In addition, Klobčar et al. investigated the FSSW of 1.6 mm and 2 mm thick 5754 aluminum alloy, measuring axial force and torque under different process parameters. They found that the axial force increased during pin penetration and when the tool shoulder contacted the workpiece, with plunge rate and rotational speed significantly affecting axial force. Torque exhibited a rise-and-fall trend, increasing with plunge rate and decreasing with rotational speed and dwell time [39]. Badwelan et al. proposed a dynamic welding process for FSSW, wherein tool rotational speed and plunge rate were dynamically adjusted at different welding stages. The welding experiments on 1050 aluminum alloy revealed that with an increasing dynamic plunge speed ratio, the maximum welding force first increased and then decreased, whereas an increasing dynamic rotation speed ratio led to a gradual decrease in maximum welding force [40]. Moreover, Tobin et al. studied the influence of preheating on the joint performance and measured the changes in axial forces and torque at different preheating temperatures during the FSSW of 2.5 mm thick 2024 aluminum alloy. The results showed that as the preheating temperature rose from room temperature to 400°C, the maximum welding force and torque decreased by 69% and 76%, respectively, due to material softening [41]. Bhardwaj et al. conducted an FSSW study on 1.5 mm thick 6061 aluminum alloy, measuring plunge force and torque at various rotational speeds. The results were compared with the forces and torques obtained from a finite element simulation model, verifying the reliability of the finite element model [42]. At present, the research on welding forces and torque has primarily focused on traditional FSSW, while few studies have examined these parameters in RFSSW, which holds great application potential but involves a more complex welding process. To improve the RFSSW process and enhance welding quality, further research is needed to reveal the variation patterns of welding forces and torque during the welding process and to establish the relationships between welding parameters and these critical forces.

Currently, measuring welding forces and torque in FSSW typically involves installing pressure and torque sensors at the bottom of the workpiece. While this method is effective in traditional FSSW, where welding times are short, heat generation is minimal, and welding forces are relatively low, it presents challenges in RFSSW, especially when applied to pure copper, which has high thermal conductivity and generates heat quickly. In the RFSSW of pure copper, traditional sensors, which are in direct contact with the workpiece, are prone to interference from high temperatures and pressures, reducing measurement accuracy and complicating installation and operation. In contrast, the octagonal ring dynamometer (ORD) offers significant advantages for measuring welding forces and torque during the RFSSW of pure copper. The ORD measures forces and torque through the mechanical deformation of the octagonal ring [43,44], and can

be isolated from the workpiece, avoiding issues related to thermal drift and high-temperature failure that affect traditional sensors. This improves measurement accuracy and operational stability. Moreover, the ORD is cost-effective, easy to use, and widely applied in force measurement in turning, milling, and drilling processes [45-48]. Therefore, using an ORD provides a feasible solution for measuring welding forces and torque in RFSSW of pure copper [49-51]. However, there are few studies on welding forces and torque in RFSSW at present, particularly a lack of research focusing on real-time force measurement during pure copper RFSSW using an octagonal ring dynamometer. To fill this gap, an ORD was designed and fabricated based on the specific requirements of the RFSSW process. The ORD was calibrated for welding forces and torque, and it was subsequently used to measure and analyze welding forces and torque during the RFSSW of pure copper. The study aimed to reveal the variations in welding forces and torque at different stages of the welding process and to establish the mathematical models that correlate welding parameters with welding forces and torque, an aspect that has not yet been elucidated in previous research on the RFSSW of pure copper. The findings of this research can provide data support for the establishment of the heat generation model for pure copper RFSSW, provide a theoretical basis for the analysis of material flow behavior during different stages of RFSSW, and serve as a reference for measuring the welding forces and torque in other types of FSSW.

2. Design of ORD

2.1. Working principle of RFSSW

The complete process of RFSSW is illustrated in Fig. 1 [52,53]. In the preheating stage, the clamping ring presses the workpiece while the pin and sleeve rotate at a constant speed. Friction between the tool and the workpiece generates heat, causing localized softening of the material, although the tool has not yet penetrated the workpiece. During the plunging stage, the sleeve plunges into the designated depth of the workpiece at a specific speed, while the pin simultaneously moves upward to a certain height. The rotation and plunging of the tool generate additional heat, further softening the material. In the dwelling stage, the sleeve and pin remain at the specified depth and height for a period of time, during which the tool continues to rotate, producing heat to soften the material further and ensure uniform mixing. In the refilling stage, the pin moves downward at a specific speed, driving the material in the stirred region to flow downward and fill the gap created by the upward movement of the sleeve. After the material is refilled, the pin and sleeve dwell on the surface of the weld for a short time to eliminate any potential voids or inconsistencies (dwelling stage II), thereby improving the weld's density. In the retracting stage, the clamping ring and tool move upward, leaving the surface of the workpiece and completing the welding process. In practical welding operations, the preheating stage and dwelling stage II may be omitted depending on the welding requirements. During the welding process, the primary welding forces include the axial force in the vertical direction (F_z), and the torque (T). Additionally, due to the mechanical stirring effect of the tool, a lateral force (F_x) is generated in the horizontal direction. This study primarily focuses on the measurement of F_z, T and F_x.

2.2. Structural design of ORD

2.2.1. Theory of force measurement with octagonal ring

The deformation of the octagonal ring under load is derived from the deformation of a thin-walled circular ring. When the radius of the ring is much larger than its wall thickness ($R \geqq 4h$), it can be treated as a thin-walled ring for analysis. Assuming the bottom of the ring is fixed, and when vertical force F_z and horizontal force F_x are applied to the top, the surface of the ring undergoes corresponding deformation, as illustrated in Fig. 2 [54,55].

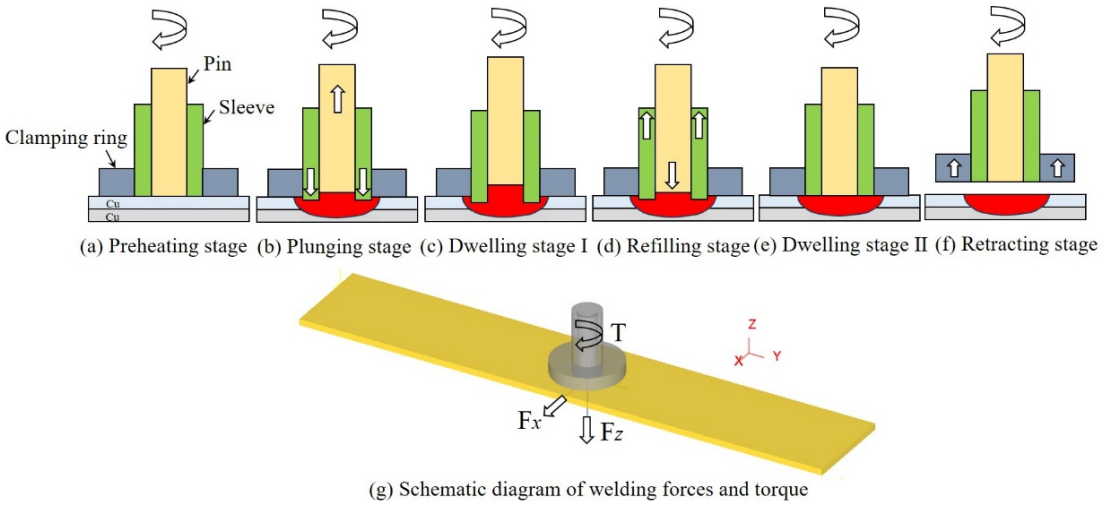

Fig. 1. Working principle of RFSSW (a-f) and schematic diagram of welding forces and torque (g)

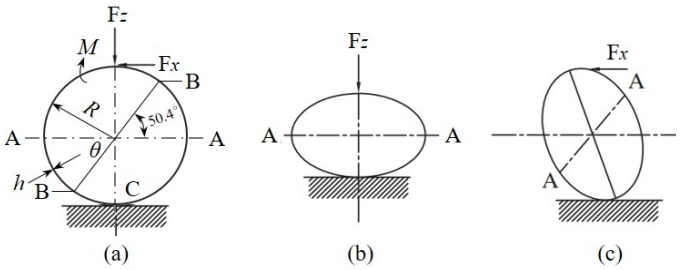

Fig. 2. Schematic diagram of the forces on the ring, (a) simplified diagram of the ring, (b) deformation under F_z, (c) deformation under F_x

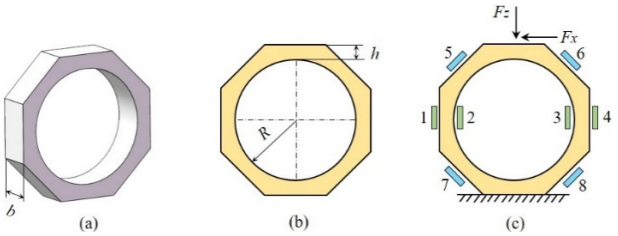

Fig. 3. Schematic diagram of the octagonal ring, (a-b) main dimensions, (c) strain gauges pasting position

After the strain gauges are attached to the surface of the ring, the external force will cause them to deform. The magnitude of the force on the ring can be calculated based on the relationship between the deformation of the strain gauges and the external force.

When F_z acts on the ring, the bending moment of any section of the ring is [56,57]:

$$M = \frac{F_z R}{2}(1-\cos\theta) - F_z R\left(\frac{1}{2}-\frac{1}{\pi}\right) = \\ = F_z R\left(\frac{1}{\pi}-\frac{\cos\theta}{2}\right) \quad (1)$$

When $\theta = 0°$, the bending moment at point A is:

$$M_A = F_z R\left(\frac{1}{\pi}-\frac{1}{2}\right) = 0.1817 F_z R \quad (2)$$

The strain at point A can be expressed as:

$$\varepsilon_A = \frac{\sigma_A}{E} = \frac{6M_A}{Ebh^2} = \frac{1.09F_z R}{Ebh^2} \quad (3)$$

where, E is the elastic modulus, b and h are the width and thickness of the ring, respectively.

When $\theta = 50.4°$, $\cos\theta = \frac{2}{\pi}$, the bending moment at point B is 0, and the strain at point B is also 0.

Similarly, when F_x acts on the ring, the strain at point A is 0, and the strain at point B is [58-60]:

$$\varepsilon_B{}' = 2.31\frac{F_x R}{Ebh^2} \quad (4)$$

Based on this principle, the strain gauges can be attached at location A to measure the vertical force F_z and at location B to measure the horizontal force F_x.

To enhance measurement stability and facilitate the attachment of strain gauges, the ring is typically designed as an octagonal ring [61,62], as shown in Fig. 3. On the octagonal ring, the strain gauges are typically affixed at an angle of 45°, where they are approximately unaffected by F_z [63]. When the angle is 45°, the strain at point B can be expressed as:

$$\varepsilon_B{}'' = 2.18\frac{F_x R}{Ebh^2} \quad (5)$$

By attaching strain gauges 1, 2, 3, and 4 to the ring, the magnitude of F_z can be measured, while strain gauges 5, 6, 7, and 8 can be used to measure F_x.

Previous studies have demonstrated that the arrangement of the octagonal ring and strain gauges can also be used to measure torque acting on the ring. When T is applied, the strain induced by the T along the horizontal centerline of the octagonal ring can be expressed as [64]:

$$\varepsilon_T = \frac{3T}{Ebh^2} \times \frac{0.36K + 0.137}{K^2 + 1.27K + 0.5} \quad (6)$$

Where, $K = \frac{L}{2R}$, L is the center distance between the rings, and R is the radius of the ring. Generally, a reasonable K value is in the range of 1.5 ~ 2.5 [65].

2.2.2. Main structural parameters of the octagonal ring

To ensure optimal measurement performance, it is essential to determine the appropriate structure and material for the octagonal ring [66]. Previous studies have indicated that for the dynamometer to achieve high sensitivity and stiffness, the thickness-to-radius ratio (h/R) of the octagonal ring should not be less than 0.25 [67,68]. Based on this, the radius R of the octagonal ring in this study was designed to be 32 mm, and the thickness h was set at 8 mm. Although the width b of the octagonal ring has little impact on the stiffness of the dynamometer, excessive width can reduce its sensitivity [69]. Therefore, the width b was designed to be 20 mm to balance installation and strain gauge attachment requirements. To ensure structural stability, the ORD's working platform is supported by four octagonal rings, with a center distance of 120 mm. Considering factors such as the size of the workpiece during welding, the dimensions and installation position of the fixtures, and the installation depth of the bolts, the working platform's length, width, and thickness were set to 200 mm, 156 mm, and 30 mm, respectively. The measurement area is defined as a circular region with a diameter of 120 mm, centered on the working platform. Due to the constraints imposed by the measurement dimensions of the working platform and the position of the octagonal rings, the designed ORD is primarily intended for measuring RFSSW at a fixed location, with the welding position preferably placed at the center of the working

platform. However, it presents certain limitations for measuring FSW processes with larger welding travel distances. The material used for the ORD is 45 steel, which is an ideal material for octagonal ring dynamometer due to its excellent comprehensive performance, economy and good process adaptability. The mechanical properties of 45 steel are listed in TABLE 1.

TABLE 1

Mechanical properties of 45 steel

Modulus of elasticity	Tensile strength	Yield strength	Poisson's ratio	Carbon content	Hardness
210 GPa	600 MPa	355 MPa	0.31	0.42~0.50%	195 HV

2.2.3. Strength verification of the octagonal ring

In the RFSSW of pure copper, the welding forces mainly arise from the clamping force of the clamping ring and the downward force of the tool, while the horizontal lateral force is relatively small. Assuming the maximum forces exerted on the load-bearing surface of the dynamometer are 20000 N in the vertical direction, 5000 N in the lateral direction, and the maximum torque is 60 N·m, the load borne by each octagonal ring is 5000 N, 1250 N, and 15 N·m, respectively. The elastic strain produced by the octagonal ring under the forces F_z, F_x, and torque T is:

$$\varepsilon_z = \pm\frac{1.09F_zR}{Ebh^2} = \frac{1.09\times5000\times32}{210000\times20\times8^2} = 6.5\times10^{-4} \tag{7}$$

$$\varepsilon_x = \pm\frac{2.18F_xR}{Ebh^2} = \frac{2.18\times1250\times32}{210000\times20\times8^2} = 3.2\times10^{-4} \tag{8}$$

$$\varepsilon_T = \frac{3T}{Ebh^2}\times\frac{0.36K+0.137}{K^2+1.27K+0.5} = \\ = \frac{3\times15000}{210000\times20\times8^2}\times\frac{0.36\times1.875+0.137}{1.875^2+1.27\times1.875+0.5} = \\ = 2.1\times10^{-5} \tag{9}$$

The stresses generated by F_z, F_x and T are:

$$\sigma_z = E\varepsilon_z = 210000\times6.5\times10^{-4} = 136.5 \text{ MPa} \tag{10}$$

$$\sigma_x = E\varepsilon_x = 210000\times3.2\times10^{-4} = 67.2 \text{ MPa} \tag{11}$$

$$\sigma_T = E\varepsilon_T = 210000\times2.1\times10^{-5} = 4.4 \text{ MPa} \tag{12}$$

The allowable stress of the material can be calculated from the yield strength and the safety factor, namely:

$$[\sigma] = \frac{\sigma_s}{s} \tag{13}$$

When the safety factor is 1.5, the allowable stress is 236.37 MPa. Therefore, the maximum stress experienced by the octagonal ring in all directions is below the allowable stress of the material, meeting safety requirements [70].

To avoid resonance during the RFSSW process, the natural frequency of the ORD should be at least four times that of the welding machine [71,72]. The natural frequency of the ORD can be expressed as [54]:

$$f_{Dynamometer} = \frac{1}{2\pi}\sqrt{\frac{K_1}{m}} \tag{14}$$

where, K_1 is the ring constant of the ORD, and m is the mass of the ORD. K_1 can be expressed as:

$$K_1 = \frac{F_z}{\delta_z} = \frac{Ebh^3}{1.8R^3} = \\ = \frac{210000\times20\times8^3}{1.8\times32^3} = 36458.3 \text{ N/mm} \tag{15}$$

Thus, the natural frequency of the ORD is:

$$f_{Dynamometer} = \frac{1}{2\pi}\sqrt{\frac{K_1}{m}} = \\ = \frac{1}{2\times3.14}\sqrt{\frac{36458.3\times1000}{18}} = 226.6 \text{ Hz} \tag{16}$$

The maximum rotational speed of the welding machine is 2000 rpm. To facilitate comparison with the natural frequency, the rotational speed needs to be converted into frequency by using the following formula:

$$f_{Welding\ machine} = \frac{n}{60} = \frac{2000\,\text{rpm}}{60} = 33.33 \text{ Hz} \tag{17}$$

Therefore, $f_{Dynamometer} > 4f_{Welding\ machine}$, indicating that the ORD will not resonate during use.

2.3. Arrangement of the octagonal ring and construction of the Wheatstone bridge

To measure the F_z, F_x, and T, twelve strain gauges were affixed to the four octagonal rings, as shown in Fig. 4. Strain

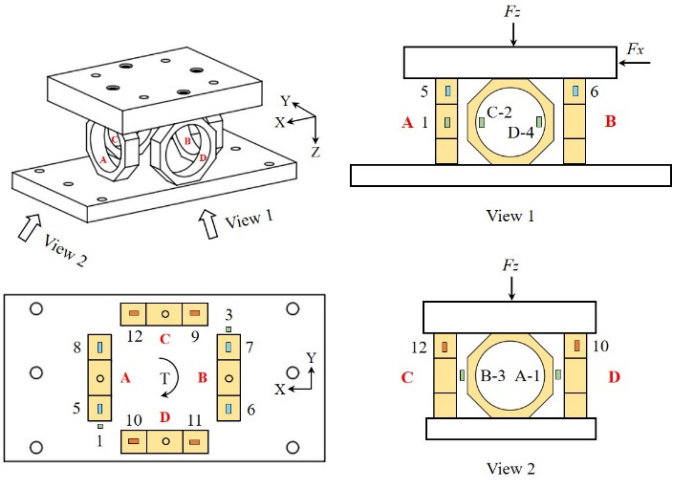

Fig. 4. Schematic diagram of octagonal ring arrangement and strain gauge pasting

gauges 1, 2, 3, and 4 were used to measure F_z, strain gauges 5, 6, 7, and 8 were used to measure T, and strain gauges 9, 10, 11, and 12 were used to measure F_x. The connection method of the Wheatstone bridge is shown in Fig. 5, and the resistance value of the strain gauges used is 120 Ω. When a load in a certain direction is applied to the ORD, the voltage and microstrain at the output end of the bridge can be obtained. The calculation process can be found in references [73,74].

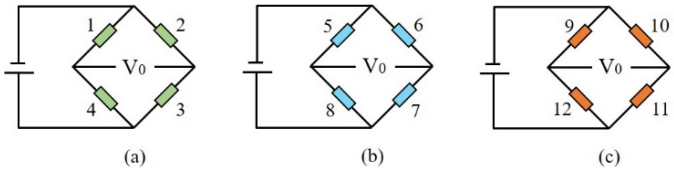

Fig. 5. Schematic diagram of bridge connection, (a) F_z, (b) T, (c) F_x

Three bridge boxes were employed to connect the twelve strain gauges designated for measuring F_z, F_x, and T, respectively, as shown in Fig. 6.

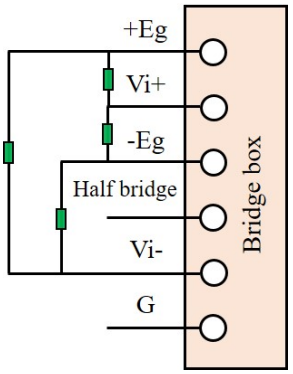

Fig. 6. Wiring diagram of strain gauges in bridge box

3. Calibration of ORD

3.1. Calibration principle

Since the fundamental principle of the ORD is to indirectly calculate the welding forces and torque through the microstrain caused by external loads, it is necessary to calibrate the ORD before measuring the welding forces and torques. A pressure sensor with a range of 0-10000 N was used for calibrating the F_z and F_x, and a torque sensor with a range of 0-200 N·m was used to calibrate the T. During calibration, the machine tool spindle applied specified forces F_z, F_x and torque T to the load-bearing surface of the ORD. A dynamic signal testing and analysis system was employed to collect the microstrain signals generated under different F_z, F_x, and T loads, with a data acquisition frequency of 500 Hz. The calibration process of the ORD is shown in Fig. 7.

In RFSSW of pure copper, the downward pressure exerted by the clamping ring is approximately 7000 N, and the axial force is significantly higher than the transverse force. Combining the

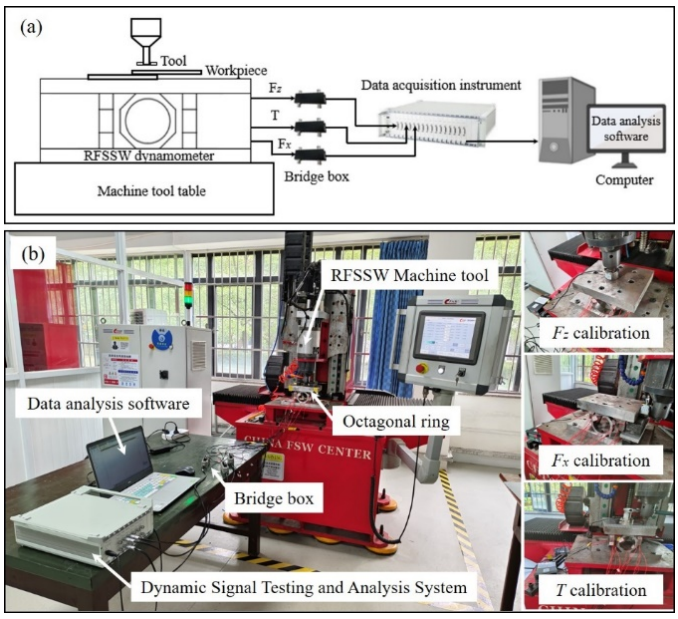

Fig. 7. Schematic diagram of ORD calibration, (a) calibration principle diagram, (b) calibration site diagram

range of the pressure and torque sensors, the calibration range for welding forces and torque in different directions was determined. To achieve high calibration accuracy, eight calibration points were selected for each direction, as shown in TABLE 2. To reduce measurement errors, each loading value was measured three times, and the arithmetic mean was taken as the final result.

TABLE 2

Settings for loading values in different directions

Loading direction	**Loading value (N/N·m)**								
F_z	0	1000	2000	3000	4000	5000	6000	7000	8000
T	0	20	40	60	80	100	120	140	160
F_x	0	500	1000	1500	2000	2500	3000	3500	4000

3.2. Analysis of calibration results

Fig. 8 shows the microstrain variation under different load directions. Microstrain refers to a unit of strain measurement, where 1 microstrain (με) equals a deformation of 1 part per million. This level of precision is critical for accurately capturing the small deformations experienced by materials under load, which is essential for measuring welding forces. It can be seen that the microstrain response values in each direction exhibited an approximately linear relationship with the applied loads. When measuring in one direction, the response values in the other two directions were relatively small, indicating that the measurement system was capable of accurately measuring the target quantities.

By performing linear fitting between the applied loads and the corresponding microstrain data, the equations describing

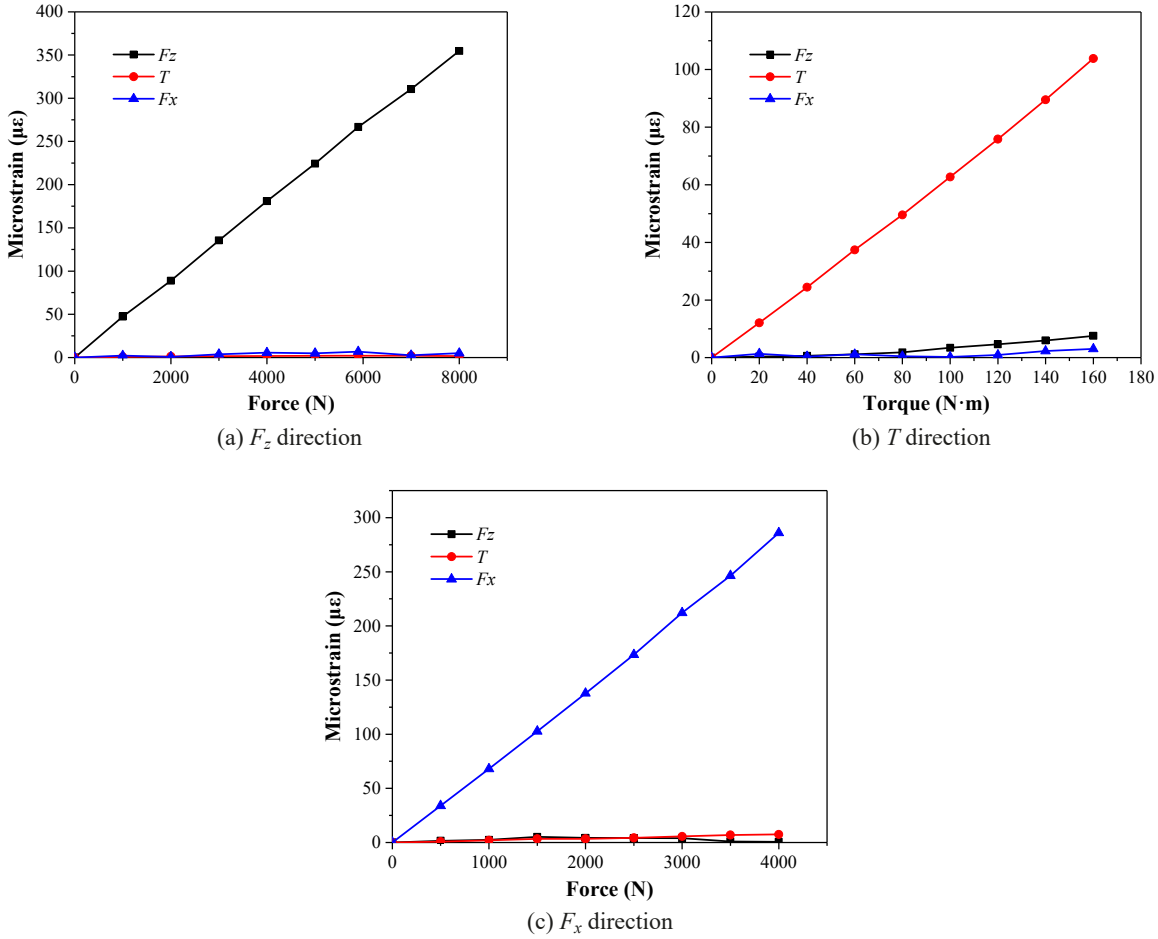

(a) F_z direction (b) T direction

(c) F_x direction

Fig. 8. Calibration results under different load directions

the relationship between strain and force in different directions can be obtained as follows:

$$\mu\varepsilon_{Fz} = 0.04436F_z + 1.84607, R^2 = 0.99975 \quad (18)$$

$$\mu\varepsilon_{T} = 0.64656T - 1.12252, R^2 = 0.9994 \quad (19)$$

$$\mu\varepsilon_{Fx} = 0.07135F_x - 2.65674, R^2 = 0.99957 \quad (20)$$

The fitting results showed that the coefficients of determination (R^2) for F_z, T, and F_x were all above 0.999, demonstrating a strong linear correlation between the strain and the applied forces for the ORD.

3.3. Verification of calibration results

To verify the calibration results further, three repeated measurements of strain values under different loading conditions were conducted, with the average value taken as the final measurement result, as shown in TABLE 3.

From TABLE 3, it can be observed that the average measurement error for F_z is 0.97%, for T is 3.78%, and for F_x is 1.56%, all of which are within 5%. This error seems to be acceptable. In FSSW or FSW, the welding force is large, and a small error has little effect on the material flow and forming quality of the welding area, which is considered to be within an acceptable range in the welding process of aluminum alloys [75]. In addition, in the measurement of cutting force, a measurement error within 5% is also considered acceptable [45].

TABLE 3

ORD test results

Loading direction	Loading value (N/N·m)	Test value (με)	Calibration value (με)	Error (%)	Average error (%)
F_z	1500	68.18	68.39	0.31	0.97
	3500	154.98	157.11	1.36	
	5500	242.77	245.83	1.24	
T	30	17.36	18.27	4.98	3.78
	70	42.50	44.14	3.72	
	110	68.15	69.99	2.63	
F_x	750	49.39	50.86	2.89	1.56
	1750	120.57	122.21	1.34	
	2750	194.45	193.56	0.46	

TABLE 4 presents the results of the cross-sensitivity tests for the ORD in different directions. Cross-sensitivity refers to the cross influence in other directions when measuring a load in a specific direction. A lower degree of cross-sensitivity indicates minimal interference to non-measurement directions, thereby enhancing the accuracy and effectiveness of the measurement.

TABLE 4

Cross-sensitivity test results of ORD

Loading direction	Loading value (N/N·m)	Test value ($\mu\varepsilon$)			Average error of cross-sensitivity (%)					
		F_z	T	F_x	F_z		T		F_x	
F_z	1500	68.18	0.33	2.73	—		0.48	0.53	4.00	3.72
	3500	154.98	1.06	5.24	—		0.68		3.38	
	5500	242.77	1.01	9.19	—		0.42		3.79	
T	30	0.64	17.36	0.70	3.69	4.90	—		4.03	2.01
	70	2.07	42.50	0.73	4.87		—		1.72	
	110	4.18	68.15	0.19	6.13		—		0.28	
F_x	750	2.12	0.27	49.39	4.29	3.31	0.55	0.84	—	
	1750	3.86	0.92	120.57	3.20		0.76		—	
	2750	4.73	2.37	194.45	2.43		1.22		—	

The observations reveal that the cross-sensitivity error in each direction is within 5%, indicating minimal interference from other directions when measuring in a specific direction. Thus, the constructed ORD demonstrates high measurement precision and is suitable for measuring welding forces and torque during the RFSSW of pure copper.

4. Measurement of welding forces and torque in RFSSW of pure copper

In RFSSW, the plunge depth (PD), rotational speed (RS), and dwell time (DT) are the main factors affecting the welding forces and torque. Using the calibrated ORD, measurements were conducted on 27 sets of welding experiments under varying PDs, RSs, and DTs, with the detailed process parameters provided in TABLE 5. The welding experiments were carried out using a FSW-TS-DH04 tabletop RFSSW equipment produced by China Friction Stir Welding Center. The tool was made of SKH-9 high-speed steel. The diameter of the pin and the sleeve was 6 mm and 9 mm, respectively. In these welding experiments, the pressure of the clamping ring was set at 7000 N, and both the preheating time and the dwell time II were 3 s. The dimensions of the pure copper sheets were 100×30×1 mm, with an overlap size of 30×30 mm for the top and bottom sheets.

TABLE 5

Process parameter settings for welding forces and torque measurement

No.	PD (mm)	RS (rpm)	DT (s)	No.	PD (mm)	RS (rpm)	DT (s)
1	0.6	800	2	15	1.1	1200	6
2	0.6	800	4	16	1.1	1600	2
3	0.6	800	6	17	1.1	1600	4
4	0.6	1200	2	18	1.1	1600	6
5	0.6	1200	4	19	1.6	800	2
6	0.6	1200	6	20	1.6	800	4
7	0.6	1600	2	21	1.6	800	6
8	0.6	1600	4	22	1.6	1200	2
9	0.6	1600	6	23	1.6	1200	4
10	1.1	800	2	24	1.6	1200	6
11	1.1	800	4	25	1.6	1600	2
12	1.1	800	6	26	1.6	1600	4
13	1.1	1200	2	27	1.6	1600	6
14	1.1	1200	4				

4.1. Typical variation patterns of welding forces and torque

Fig. 9 illustrates the variation in welding forces and torque under the conditions of a PD of 1.1 mm, a RS of 1200 rpm, and

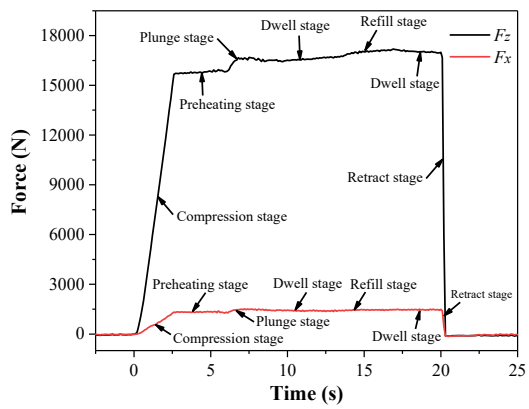

(a) Welding forces

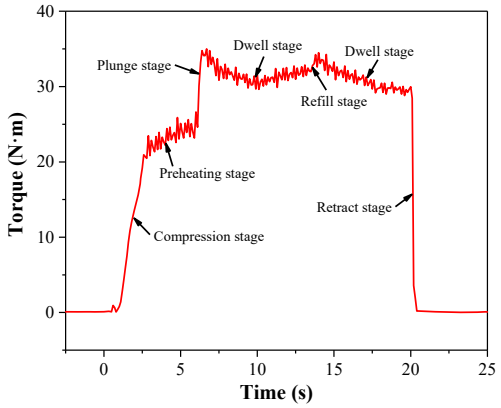

(b) Torque

Fig. 9. Typical variation patterns of welding forces and torque in RFSSW

a DT of 4 s. It can be observed that F_z is significantly larger than F_x, with the peak value of F_z reaching 11.3 times that of F_x. During the compression stage, the welding forces increase as the clamping ring and rotating tool continue to exert downward pressure. The increased contact area and friction between the tool and the workpiece also lead to a rise in torque. In the preheating stage, the clamping ring applies a certain pressure to the workpiece, and the tool rotates at high speed, contacting the welding surface. As the temperature rises, the material in the preheated area begins to soften, increasing the frictional resistance on the tool, leading to a slight increase in both welding forces and torque. In the plunging stage, as the PD increases, the contact area between the tool and the workpiece continues to grow. The material is mechanically compressed by the tool, resulting in plastic deformation, which increases the resistance of the material and causes a rapid rise in welding forces. At this point, the torque shows a trend of rapid increase followed by a gradual decrease. Initially, as the tool penetrates the unsoftened interior of the material, the mechanical resistance and friction increase sharply, causing the torque to rise. However, as the tool penetrates deeper, the generated frictional heat spreads to the deeper areas of the weld, further softening the material and enhancing its flowability, which reduces friction and mechanical resistance, causing the torque to decrease gradually. During the dwell stage, the tool remains at a specific PD while rotating, further softening the material through friction-generated heat. As the material's flow resistance decreases, both the welding forces and torque show a slight decline. In the refilling stage, the material in the stirred zone flows downward under the action of the tool pin, intensifying plastic deformation, leading to another increase in welding forces and torque. During the dwell stage II, with no vertical force acting on the workpiece and the material softening further, both welding forces and torque show a slight decrease. In the retracting stage, the tool and clamping ring lift off the workpiece, causing the welding forces and torque to drop sharply. The maximum welding forces occur near the dwell stage II, just before the welding process is completed, while the peak torque occurs during the plunging stage.

4.2. Mathematical model of welding forces and torque

The maximum forces and torque generated during the welding process have a significant impact on weld quality, the reliability of welding equipment and fixtures, and the lifespan of the tool. These are critical factors that warrant close attention. Since the welding forces and torque are closely related to process parameters, it is essential to establish a relationship between them and the welding process parameters. TABLE 6 lists the maximum welding forces and torque under different welding process parameters.

Through regression analysis, the relationship between welding process parameters and welding forces and torque can be established. In the field of engineering technology, second-order polynomials are commonly used to fit independent and dependent variables, providing sufficient accuracy [58]. The relationships between the maximum F_z, T, F_x, and the welding process parameters can be expressed as:

TABLE 6

Measurement results of welding forces and torque

No.	F_z (N)	T (N·m)	F_x (N)	No.	F_z (N)	T (N·m)	F_x (N)
1	16770.38	40.35	1583.54	15	17606.91	36.49	1564.81
2	16807.43	33.06	1488.78	16	17489.86	33.67	1497.85
3	16959.01	33.56	1531.46	17	17591.69	33.99	1653.57
4	16871.04	29.29	1401.00	18	17753.24	37.82	1573.82
5	16832.31	30.42	1478.99	19	17210.95	41.85	1438.78
6	16837.66	32.04	1408.31	20	17108.28	36.78	1389.97
7	16781.92	31.14	1443.22	21	17183.13	37.40	1393.62
8	16858.97	27.21	1372.15	22	17220.08	33.30	1387.94
9	17101.15	33.08	1358.77	23	17387.72	37.30	1538.38
10	17018.53	34.23	1494.72	24	17525.03	34.19	1494.13
11	17020.32	34.53	1462.61	25	17411.76	33.61	1423.19
12	17103.35	35.06	1580.6	26	17620.55	38.13	1563.77
13	17168.96	34.13	1564.16	27	17915.32	34.35	1657.55
14	17185.65	35.01	1519.97				

$$\begin{cases} F_z = a_0 + a_1 PD + a_2 RS + a_3 DT + a_{12} PD \cdot RS \\ \quad + a_{13} PD \cdot DT + a_{23} RS \cdot DT + a_{11} PD^2 \\ \quad + a_{22} RS^2 + a_{33} DT^2 \\ T = a_0 + a_1 PD + a_2 RS + a_3 DT + a_{12} PD \cdot RS \\ \quad + a_{13} PD \cdot DT + a_{23} RS \cdot DT + a_{11} PD^2 \\ \quad + a_{22} RS^2 + a_{33} DT^2 \\ F_x = a_0 + a_1 PD + a_2 RS + a_3 DT + a_{12} PD \cdot RS \\ \quad + a_{13} PD \cdot DT + a_{23} RS \cdot DT + a_{11} PD^2 \\ \quad + a_{22} RS^2 + a_{33} DT^2 \end{cases} \tag{21}$$

By substituting the values from TABLE 6 into the above equation and performing regression analysis using SPSS software, the coefficients of the second-order polynomial can be obtained. The resulting mathematical models are as follows:

$$\begin{cases} F_z = 16646.335 + 1505.683 PD - 0.817 RS \\ \quad - 198.927 DT + 0.517 PD \cdot RS + 25.518 PD \cdot DT \\ \quad + 0.088 RS \cdot DT - 772.073 PD^2 + 0.000151 RS^2 \\ \quad + 15.312 DT^2 \\ T = 56.343 + 7.782 PD - 0.034 RS - 3.433 DT \\ \quad + 0.002 PD \cdot RS - 0.06 PD \cdot DT + 0.002 RS \cdot DT \\ \quad - 2.844 PD^2 + 0.000008847 RS^2 + 0.176 DT^2 \\ F_x = 1863.059 + 176.135 PD - 0.625 RS - 44.013 DT \\ \quad + 0.355 PD \cdot RS + 35.384 PD \cdot DT + 0.025 RS \cdot DT \\ \quad - 326.816 PD^2 + 0.00006687 RS^2 - 1.929 DT^2 \end{cases} \tag{22}$$

The coefficients of determination R^2 for the equations of F_z, T, and F_x are 0.933, 0.583, and 0.709, respectively, indicat-

ing that PD, RS, and DT account for 93.3% of the variation in F_z, 58.3% of the variation in T, and 70.9% of the variation in F_x. Overall, the models explain most of the variation in welding forces and torque. The Durbin-Watson statistics for the F_z, T, and F_x equations are 0.966, 1.980, and 2.494, respectively. The Durbin-Watson statistic is used to test for autocorrelation in the residuals of the regression model, and values within the range of 0-4 are considered reasonable. In this study, the Durbin-Watson values for F_z, T, and F_x are within the acceptable range, indicating that the observations in the regression model are independent of one another.

The results of variance analysis for the models are shown in TABLE 7.

The F-values in variance analysis test the overall significance of the regression models, reflecting the extent to which the welding process parameters as a whole influence welding forces and torque. The significance level associated with the F-value helps evaluate the statistical significance of the regression analysis, which is generally considered significant if the value is less than 0.05. As shown in TABLE 7, the significance values for the F_z, T, and F_x models are all below 0.05, indicating that the regression models are statistically significant, meaning that the welding process parameters have a significant impact on welding forces and torque.

In the regression model, each independent variable has a corresponding t-value, which reflects the degree of influence the independent variable has on the dependent variable. The larger the absolute value of the t-value, the more significant the effect of the independent variable on the dependent variable. Typically, the significance of an independent variable can be determined by the absolute value of the t-value and its corresponding significance value. The absolute values of the t-values and their significance levels for each independent variable are shown in TABLE 8.

In the F_z model, the PD^2 term has the largest absolute t-value and the smallest significance value, indicating that the PD^2 term has the most significant influence on F_z. The PD term has a t-value of 3.469 and a significance value of 0.003, making it the second most significant factor influencing F_z. This shows that PD has the greatest impact on F_z, with the PD · RS and RS · DT terms also significantly affecting F_z (with a significance value less than 0.05). The RS^2 term has the least impact on F_z. In the T model, the RS term has the largest absolute t-value and the smallest significance value, indicating that RS has the most significant effect on T. The PD · DT term has the smallest absolute t-value and the largest significance value, showing that it has the least effect on T. In the F_x model, the PD · RS term has the largest absolute t-value and the smallest significance value, indicating that this term has the most significant influence on F_x. The PD^2 term and the PD · DT term also significantly affect F_x, while the DT^2 term has the least impact on F_x.

4.3. Validation of mathematical models

To validate the regression models, welding force and torque measurement experiments were repeated under three different sets of process parameters. For each set, three measurements were taken, and the average of the maximum values of welding forces and torque from the three tests was used as the test result. The experimental results are presented in TABLE 9.

TABLE 7

Results of variance analysis

Model	Sources of variance	Sum of squares	Degrees of freedom	Mean square	F	Significance
F_z	Regression	2557097.155	9	284121.906	26.335	< 0.001
	Residual	183407.961	17	10788.704		
	Total	2740505.116	26			
T	Regression	152.388	9	16.932	2.646	0.040
	Residual	108.790	17	6.399		
	Total	261.177	26			
F_x	Regression	131786.449	9	14642.939	4.598	0.003
	Residual	54139.348	17	3184.668		
	Total	185925.797	26			

TABLE 8

Absolute values of the t-values and significance

Model		PD	RS	DT	PD · RS	PD · DT	RS · DT	PD^2	RS^2	DT^2
F_z	$\lvert t \rvert$	3.469	1.207	1.946	3.446	0.851	2.336	4.552	0.570	1.444
	Significance	0.003	0.244	0.068	0.003	0.407	0.032	<0.001	0.576	0.167
T	$\lvert t \rvert$	0.736	2.081	1.379	0.639	0.082	1.967	0.689	1.371	0.683
	Significance	0.472	0.053	0.186	0.531	0.935	0.066	0.500	0.188	0.504
F_x	$\lvert t \rvert$	0.747	1.699	0.792	4.357	2.172	1.214	3.546	0.464	0.335
	Significance	0.465	0.108	0.439	<0.001	0.044	0.242	0.002	0.648	0.742

TABLE 9

Comparison of calculated values and experimental values

Model	Welding parameters			Calculated value (N)	Experimental value (N)	Error (%)	Average error (%)
	PD	RS	DT				
F_z	0.8	1000	6	17112.51	16983.78	0.75	0.61
	1.2	1400	4	17426.66	17316.80	0.63	
	1.4	1300	2	17338.70	17258.89	0.46	
T	0.8	1000	6	34.65	35.17	1.50	2.25
	1.2	1400	4	34.68	34.48	0.58	
	1.4	1300	2	34.92	36.55	4.67	
F_x	0.8	1000	6	1507.00	1489.62	1.15	1.20
	1.2	1400	4	1559.20	1541.93	1.11	
	1.4	1300	2	1484.03	1503.71	1.33	

From TABLE 9, it can be observed that the average error between the experimental and calculated values is 0.61% for F_z, 2.25% for T, and 1.20% for F_x, with the maximum error being 4.67%. This indicates that the model predictions are highly accurate.

The established mathematical relationships between welding forces, torque, and welding process parameters can be utilized in the study of the heat generation model for RFSSW of pure copper, as well as for the validation of the finite element simulation model. It can also provide a reference for pressure values for the study of the atomic diffusion mechanism at the interface during welding. Moreover, when welding copper sheet components sensitive to pressure, such as thin-plate heat exchangers and electrical connectors, RFSSW can benefit from limiting the welding forces and torque to predict reasonable welding parameters. Future research on the measurement and analysis of FSSW forces and torque can be expanded to include additional welding types, such as swept FSSW and pinless FSSW, as well as welds between workpieces of varying thicknesses and materials, to better understand force variations under complex welding conditions. Furthermore, analyzing welding forces and torque offers a novel perspective for optimizing welding processes and reducing energy consumption in welding equipment.

5. Conclusions

In this study, the design and fabrication of a dynamometer for RFSSW of pure copper were conducted, and the welding forces and torque during the welding process were measured. The variations in welding forces and torque at different welding stages were analyzed, and mathematical models relating the maximum welding forces and torque to the welding process parameters were established. The main conclusions are as follows:

(1) The calibration errors of the dynamometer for axial force, torque, and lateral force were 0.97%, 3.78%, and 1.56%, respectively, with cross-sensitivity errors within 5%. These results demonstrate the satisfactory measurement performance of the dynamometer, ensuring its reliability for use in welding force studies.

(2) The primary welding force during the RFSSW process of pure copper was the axial force, with the peak axial force exceeding ten times the peak lateral force, which is consistent with researchers' understanding of the main welding force direction in RFSSW. The major increases in welding forces and torque occurred during the clamping, plunging, and refilling stages. The maximum welding force occurred near the second dwell stage before the end of the welding process, while the maximum torque occurred during the plunging stage. The main process parameters affecting the axial force and torque were the plunge depth and rotational speed, respectively. The lateral force was significantly influenced by the combined effects of plunge depth and rotational speed. These findings provide valuable insights for improving welding quality in practical applications, such as enhancing the reliability of electrical connectors and heat exchangers.

(3) The average prediction errors of the mathematical models for axial force, torque, and lateral force were 0.61%, 2.25%, and 1.20%, respectively. The prediction accuracy meets the expected requirements. The established mathematical models for welding forces and torque provide a useful reference for the optimization of welding process parameters and the analysis of material flow mechanisms. Further validation of these models under different welding conditions and joint configurations can expand their applicability and deepen the understanding of the welding process.

Acknowledgements

The authors gratefully acknowledge the financial support from the Key Research Project of Natural Science in Anhui Higher Education Institutions (No. 2022AH051947, No. KJ2021A1042), the Open Research Project of Anhui Simulation Design and Modern Manufacture Engineering Technology Research Center (No. SGCZXYB2302), the Anhui Province Excellent Young Teacher Cultivation Project (No. YQYB2024066), and the Research Project of Huangshan University (No. hsxyssd006). These projects provided crucial support for purchasing specialized equipment, processing dynamometer, conducting experimental trials, facilitating data analysis, etc., enabling us to achieve the research objectives outlined in this study.

REFERENCES

[1] D. Kim, S. Baek, M. Nishijima, H.C. Lee, P. Geng, N.S. Ma, Z. Zhang, H. Park, C.T. Chen, S.J. Lee, K. Suganuma, Toward defect-less and minimized work-hardening loss implementation of Al alloy/high-purity Cu dissimilar lap joints by refill friction stir spot welding for battery tab-to-busbar applications. Mater. Sci. Eng. A **892**, 146089 (2024).
DOI: https://doi.org/10.1016/j.msea.2024.146089

[2] A. Forsström, S. Bossuyt, Y. Yagodzinskyy, K. Tsuzaki, H. Hänninen, Strain localization in copper canister FSW welds for spent nuclear fuel disposal. J. Nucl. Mater. **523**, 347-359 (2019).
DOI: https://doi.org/10.1016/j.jnucmat.2019.06.024

[3] D. Ólafsson, P. Vilaça, J. Vesanko, Multiphysical characterization of FSW of aluminum electrical busbars with copper ends. Weld. World **64**, 59-71 (2020).
DOI: https://doi.org/10.1007/s40194-019-00814-0

[4] H. Zhang, K.X. Jiao, J.L. Zhang, J.P. Liu, Experimental and numerical investigations of interface characteristics of copper/steel composite prepared by explosive welding. Mater. Des. **154**, 140-152 (2018). DOI: https://doi.org/10.1016/j.matdes.2018.05.027

[5] P. Xue, G.M. Xie, B.L. Xiao, Z.Y. Ma, L. Geng, Effect of heat input conditions on microstructure and mechanical properties of friction-stir-welded pure copper. Metall. Mater. Trans. A **41**, 2010-2021 (2010). DOI: https://doi.org/10.1007/s11661-010-0254-y

[6] A. Heidarzadeh, M. Jabbari, M. Esmaily, Prediction of grain size and mechanical properties in friction stir welded pure copper joints using a thermal model. Int. J. Adv. Manuf. Technol. **77**, 1819-1829 (2015). DOI: https://doi.org/10.1007/s00170-014-6543-7

[7] Z. Barlas, Effect of friction stir spot weld parameters on Cu/CuZn30 bimetal Joints. J. Adv. Manuf. Technol. **80**, 161-170 (2015). DOI: https://doi.org/10.1007/s00170-015-6998-1

[8] A.K. Jassim, R. Al-Subar, D.Ch. Ali, Portable drilling machine applied as a friction stir tool to join light metals. Appl. Eng. Lett. **7**(4), 154-162 (2022).
DOI: https://doi.org/10.18485/aeletters.2022.7.4.3

[9] M. Kabirmohammadi, S. Yazdani, A. Ghasemi, Z.L. Peng, T. Saeid, M. Pouranvari, Insights into the microstructural evolution and strengthening mechanisms of friction stir spot welded advanced high strength ultrafine bainitic steel. Mater. Charact. **216**, 114291 (2024).
DOI: https://doi.org/10.1016/j.matchar.2024.114291

[10] V. Feizollahi, A.H. Moghadam, Effect of pin geometry, rotational speed, and dwell time of tool in dissimilar joints of low-carbon galvanized steel and aluminum 6061-T6 by friction stir spot welding. Results Mater. **20**, 100483 (2023).
DOI: https://doi.org/10.1016/j.rinma.2023.100483

[11] L. Zhou, R.X. Zhang, G.H. Li, W.L. Zhou, Y.X. Huang, X.G. Song, Effect of pin profile on microstructure and mechanical properties of friction stir spot welded Al-Cu dissimilar metals. J. Manuf. Process. **36**, 1-9 (2018).
DOI: https://doi.org/10.1016/j.jmapro.2018.09.017

[12] V. Feizollahi, M. Yousefi, A. Elahifar, B. Pourmirza, M.G. Hasab, A.H. Moghadam, Effect of shoulder diameter, tool rotation speed, and arrangement of plates on mechanical and metallurgical properties of dissimilar aluminum 2024-T3 and 7075-T6 friction stir spot welding (FSSW). Eng. Fail. Anal. **163**, 108548 (2024).
DOI: https://doi.org/10.1016/j.engfailanal.2024.108548

[13] D. Bakavos, Y.C. Chen, L. Babout, P. Prangnell, Material interactions in a novel pinless tool approach to friction stir spot welding thin aluminum sheet. Metall. Mater. Trans. A **42**, 1266-1282 (2011).
DOI: https://doi.org/10.1007/s11661-010-0514-x

[14] A. Mahgoub, A. Bazoune, N. Merah, F. Al-Badour, A. Shuaib, Effect of welding parameters on the mechanical and metallurgical properties of friction stir spot welding of copper lap joint. Arab. J. Sci. Eng. **44**(2), 1283-1292 (2019).
DOI: https://doi.org/10.1007/s13369-018-3472-z

[15] J. Seaman, K. Namola, J. Gould. Refill friction stir spot welding development, EWI (2016). https://ewi.org/wp-content/uploads/2016/10/Refill-friction-stir-spot-welding.pdf

[16] H.T. Elmetwally, M.A. Abdelhafiz, M.N. El-Sheikh, M.E. Abdullah, Effect of friction stir-welding tool pin geometry on the characteristics of Al-Cu joints,. Appl. Eng. Lett. **8** (2), 60-69 (2023).
DOI: https://doi.org/10.18485/aeletters.2023.8.2.3

[17] E. Boldsaikhan, S. Fukada, M. Fujimoto, K. Kamimuki, H. Okada, B. Duncan, P. Bui, M. Yeshiambel, B. Brown, A. Handyside. Refill friction stir spot joining for aerospace aluminum alloys. Friction Stir Welding and Processing IX, Springer (2017).
DOI: https://doi.org/10.1007/978-3-319-52383-5_23

[18] M. Fujimoto, M. Inuzuka, S. Koga, Y. Seta, Development of friction spot joining. Weld. World **49** (3-4), 18-21 (2005).
DOI: https://doi.org/10.1007/BF03266470

[19] G.S. Yu, C.H. Zhao, C.S. Liu, S.P. Guo, Y.H. Zhang, Y.F. Zhang, X. Chen, Tensile-shear mechanical properties of friction stir spot weld bonding hybrid joint in welding prior to and after adhesive curing for vehicle using. Int. J. Adhes. Adhes. **134**, 103769 (2024).
DOI: https://doi.org/10.1016/j.ijadhadh.2024.103769

[20] G. Buffa, L. Fratini, M. Piacentini, On the influence of tool path in friction stir spot welding of aluminum alloys. J. Mater. Process. Technol. **208** (1-3), 309-317 (2008).
DOI: https://doi.org/10.1016/j.jmatprotec.2008.01.001

[21] G. S. Yu, X. Chen, Z. T. Wu, Mechanical performance optimization and microstructure analysis of similar thin AA6061-T6 sheets produced by swept friction stir spot welding. Int. J. Adv. Manuf. Technol. **118**, 1829-1841 (2022).
DOI: https://doi.org/10.1007/s00170-021-07387-7

[22] Z.M. Su, R.Y. He, P.C. Lin, K. Dong, Fatigue analyses for swept friction stir spot welds in lap-shear specimens of alclad 2024-T3 aluminum sheets. Int. J. Fatigue **61**, 129-140 (2014).
DOI: https://doi.org/10.1016/j.ijfatigue.2013.11.021

[23] Z.M. Su, R.Y. He, P.C. Lin, K. Dong, Fatigue of alclad AA2024-T3 swept friction stir spot welds in cross-tension specimens. Mater. Express **236**, 162-175 (2016).
DOI: https://doi.org/10.1016/j.jmatprotec.2016.05.014

[24] S. Suresh, K. Venkatesan, E. Natarajan, S. Rajesh, W.H. Lim, Evaluating weld properties of conventional and swept friction stir spot welded 6061-T6 aluminium alloy. Mater. Express **9** (8), 851-860 (2019).
DOI: https://doi.org/10.1166/mex.2019.1584

[25] X.L. Ge, D. Jiang, W.W. Song, H.F. Hong, Effects of tool plunging path on the welded joint properties of pinless friction stir spot welding. Lubricants **11**(3), 150 (2023).
DOI: https://doi.org/10.3390/lubricants11030150

[26] M.M.Z. Ahmed, M.M. El-Sayed Seleman, E. Ahmed, H.A. Reyad, N.A. Alsaleh, I. Albaijan, A novel friction stir deposition technique to refill keyhole of friction stir spot welded AA6082-T6 dissimilar joints of different sheet thicknesses. Materials **15** (19), 6799 (2022).
DOI: https://doi.org/10.3390/ma15196799

[27] C. Schilling, J. dos Santos. Method and device for joining at least two adjoining work pieces by friction welding. US Patent, 6722556-B2 (2004).

[28] V.R. Ferrari, F.G. Coury, U.F.H. Suhuddin, N.G. Alcântara, J.F. dos Santos, R. Ohashi, M. Fujimoto, G.Y. Koga, Effects of semi-solid structure on interface formation of dissimilar aluminum to galvanized steel welds produced by load-controlled Refill Friction Stir Spot Welding. J. Manuf. Process. **84**, 298-315 (2022).
DOI: https://doi.org/10.1016/j.jmapro.2022.10.001

[29] B. Larsen, Y. Hovanski, Reducing cycle times of refill friction stir spot welding in automotive aluminum alloys. SAE Technical Paper, 2020-01-0224 (2020).
DOI: https://doi.org/10.4271/2020-01-0224

[30] A. Kubit, K. Faes, H.A. Derazkola, Refill friction stir spot welding tool plunge depth effects on shear, peel, and fatigue properties of Alclad coated AA7075 aluminum joints. Int. J. Fatigue **185**, 108308 (2024).
DOI: https://doi.org/10.1016/j.ijfatigue.2024.108308

[31] Z. Liu, Z.Y. Fan, L. Liu, S. Miao, Z.C. Lin, C.G. Wang, Y.Q. Zhao, R.L. Xin, C.L. Dong, Refill friction stir spot welding of AZ31 magnesium alloy sheets: metallurgical features, microstructure, texture and mechanical properties. J. Mater. Res. Technol. **23**, 3337-3350 (2023). DOI: https://doi.org/10.1016/j.jmrt.2023.01.151

[32] Y.F. Zou, W.Y. Li, X.W. Yang, Y. Su, Q. Chu, Z.K. Shen, Microstructure and mechanical properties of refill friction stir spot welded joints: Effects of tool size and welding parameter. J. Mater. Res. Technol. **21**, 5066-5080 (2022).
DOI: https://doi.org/10.1016/j.jmrt.2022.11.108

[33] M. Wu, C.S. Wu, S. Gao, Effect of ultrasonic vibration on fatigue performance of AA 2024-T3 friction stir weld joints. J. Manuf. Process. **29**, 85-95 (2017).
DOI: https://doi.org/10.1016/j.jmapro.2017.07.023

[34] D. Trimble, J. Monaghan, G.E. O'Donnell, Force generation during friction stir welding of AA2024-T3. CIRP Ann. **61** (1), 9-12 (2012).
DOI: https://doi.org/10.1016/j.cirp.2012.03.024

[35] A.K. Pattanaik, L.P. Nayak, R.K. Bisoyi, K. Pal, D. Mishra, Monitoring of friction stirred spot weld quality for dissimilar Al6061 to polycarbonate using tool assisted thrust-torque signatures. J. Mech. Eng. Sci. **238** (2), 515-542 (2024).
DOI: https://doi.org/10.1177/09544062231173

[36] D.G. Andrade, S. Sabari, I. Galvão, C. Leitão, D.M. Rodrigues, Temperature and torque in FSSW of steel sheets: experimental measurements and modelling. Weld. World **67**, 341-352 (2023).
DOI: https://doi.org/10.1007/s40194-022-01418-x

[37] S. Das, R.G. Narayanan, Friction stir spot welding of aluminum and steel sheets using a consumable sheet. Int. J. Adv. Manuf. Technol. **128**, 221-241 (2023).
DOI: https://doi.org/10.1007/s00170-023-11863-7

[38] A.E. Ragab, A. Alsaty, A. Alsamhan, A.A. Al-Tamimi, A. Dabwan, A. Sayed, W. Alghilan, Open-source real-time monitoring system of temperature and force during friction stir spot welding. J. Eng. Res. (2023) (In Press).
DOI: https://doi.org/10.1016/j.jer.2023.08.020.

[39] D. Klobčar, J. Tušek, A. Skumavc, A. Smolej, Parametric study of friction stir spot welding of aluminium alloy 5754. Metalurgija **53** (1), 21-24 (2014).
https://hrcak.srce.hr/104365

[40] A. Badwelan, A.M. Al-Samhan, S. Anwar, L. Hidri, Novel technique for enhancing the strength of friction stir spot welds through dynamic welding parameters. Metals **11**, 280 (2021).
DOI: https://doi.org/10.3390/met11020280

[41] D. Tobin, S. O'Shaughnessy, D. Trimble, Characterisation of force and torque with auxiliary heating during friction stir spot welding of AA2024-T3. Results Mater. **21**, 100535 (2024).
DOI: https://doi.org/10.1016/j.rinma.2024.100535

[42] N. Bhardwaj, R. Ganesh Narayanan, U.S. Dixit, Experimental and numerical investigation on the effect of rotational speed on exit-hole-free friction stir spot welding with consumable pin. Int. J. Mater. Form. **16** (54), 1-14 (2023).
DOI: https://doi.org/10.1007/s12289-023-01779-8

[43] M.S. Uddin, S.Y. Dong, On the design and analysis of an octagonal-ellipse ring based cutting force measuring transducer. Measurement **90**, 168-177 (2016).
DOI: https://doi.org/10.1016/j.measurement.2016.04.055

[44] Y. Zhao, Y.L. Zhao, S.B. Liang, G.W. Zhou, A high performance sensor for triaxial cutting force measurement in turning. Sensors **15**, 7969-7984 (2015).
DOI: https://doi.org/10.3390/s150407969

[45] T. Mohanraj, M. Uddin, S.K. Thangarasu, Review on sensor design for cutting force measurement. J. Process Mech. Eng. **237** (2), 455-466 (2023).
DOI: https://doi.org/10.1177/09544089221106264

[46] S. Karabay, Analysis of drill dynamometer with octagonal ring type transducers for monitoring of cutting forces in drilling and allied process,. Mater. Des. **28** (2), 673-685, (2007).
DOI: https://doi.org/10.1016/j.matdes.2005.07.008

[47] P. Wang, Y.J. Yang, R.J. Zhao, F. Yang, N. Wang. C.M. Zhang, Y.X. Liang, Research on orthogonal decagonal ring 3-D cutting force sensor,. IEEE Sens. J. **23** (2), 1042-1051 (2023).
DOI: https://doi.org/10.1109/JSEN.2022.3218650

[48] T. Mohanraj, S. Shankar, R. Rajasekar, M.S. Uddin, Design, development, calibration, and testing of indigenously developed strain gauge based dynamometer for cutting force measurement in the milling process. J. Mech. Eng. Sci. **14** (2), 6594-6609 (2020).
DOI: https://doi.org/10.15282/jmes.14.2.2020.05.0517

[49] D. Bipul, P. Sukhomay, B. Swarup, Design and development of force and torque measurement setup for real time monitoring of friction stir welding process. Measurement **103**, 186-198 (2017).
DOI: https://doi.org/10.1016/j.measurement.2017.02.034

[50] B. Parida, S.D. Vishwakarma, S. Pal, Design and development of fixture and force measuring system for friction stir welding process using strain gauges. J. Mech. Sci. Technol. **29** (2), 739-749 (2015). DOI: https://doi.org/10.1007/s12206-015-0134-x

[51] H.F. Wang, J.L. Wang, D.W. Zuo, W.W. Song, Application of stir tool force measuring dynamometer for friction stir welding of aluminum alloys. Strength Mater. **49** (1), 162-170 (2017). DOI: https://doi.org/10.1007/s11223-017-9854-8

[52] D. Chen, J.L. Li, J.T. Xiong, J.M. Shi, J.X. Dou, H.X. Zhao, Enhance mechanical properties of refill friction stir spot welding joint of alclad 7050/2524 aluminum via suspension rotating process. J. Mater. Res. Technol. **12**, 1243-1251 (2021). DOI: https://doi.org/10.1016/j.jmrt.2021.03.067

[53] Z.K. Shen, Y.Q. Ding, W. Guo, W.T. Hou, X.C. Liu, H.Y. Chen, F.J. Liu, W.Y. Li, A. Gerlich, Refill friction stir spot welding al alloy to copper via pure metallurgical joining mechanism. Chin. J. Mech. Eng. **34**, 75 (2021). DOI: https://doi.org/10.1186/s10033-021-00593-0

[54] S. Yaldız, F. Ünsaçar, Design, development and testing of a turning dynamometer for cutting force measurement. Mater. Des. **27** (10), 839-846 (2006). DOI: https://doi.org/10.1016/j.matdes.2005.04.001

[55] Q. Guo, Z.X. Zhao, X.D. Xue, X.Y. Pan, Optimal design of strain dynamometer based on CCD method. Modul. Mach. Tool Autom. Manuf. Technol. **4**, 139-142 (2021). DOI: https://doi.org/10.13462/j.cnki.mmtamt.2021.04.033

[56] G.S.M. van Stratan, N. Khandoker, S. Islam, On development of a ring type mechanical force transducer: Shape optimization, modification and characterization with different optimization codes. Measurement **171**, 108764 (2021). DOI: https://doi.org/10.1016/j.measurement.2020.108764

[57] M.Y. Liu, S. Xiao, Y. Kang, H. Song, Strain coupling characteristic analysis of octagonal ring dynamometer. Mach. Des. Manuf. **1**, 138-141 (2019). DOI: https://doi.org/10.19356/j.cnki.1001-3997.2019.01.036

[58] S. Yaldız, F. Ünsaçar, H. Sağlam, H. Işık, Design, development and testing of a four-component milling dynamometer for the measurement of cutting force and torque. Mech. Syst. Signal Process. **21** (3), 1499-1511 (2007). DOI: https://doi.org/10.1016/j.ymssp.2006.06.005

[59] S.E. Oraby, D.R. Hayhurst, High-capacity compact three-component cutting force dynamometer. Int. J. Mach. Tools Manuf. **30** (4), 549-559 (1990). DOI: https://doi.org/10.1016/0890-6955(90)90006-5

[60] S. Yaldız, F. Ünsaçar, A dynamometer design for measurement the cutting forces on turning. Measurement **39** (1), 80-89 (2006). DOI: https://doi.org/10.1016/j.measurement.2005.07.008

[61] S. Karabay, Design criteria for electro-mechanical transducers and arrangement for measurement of strains due to metal cutting forces acting on dynamometers. Mater. Des. **28** (2), 496-506 (2007). DOI: https://doi.org/10.1016/j.matdes.2005.08.014

[62] M.J. O'Dogherty, The design of octagonal ring dynamometers. J. Agric. Eng. Res. **63** (1), 9-18 (1996). DOI: https://doi.org/10.1006/jaer.1996.0002

[63] W.X. Wei, Analysis of coupling characteristic for milling force measurement based on octagonal rings. Master's Thesis, Wuhan University of Technology, Wuhan (2015).

[64] T.C. Thakun, R.J. Godwin, Design of extended octagonal ring dynamometer for rotary tillage studies, Agric. Mech. Asia Afr. Lat. Am. **19** (3), 23-28 (1988). https://api.semanticscholar.org/CorpusID:111629386

[65] J.L. Zhang, Research on transducer of rotary blades. J. Transducer Technol. **20** (7), 14-16 (2001). DOI: https://doi.org/10.13873/j.1000-97872001.07.004

[66] J. Tlusty, G.C. Andrews, A critical review of sensors for unmanned machining. CIRP Ann. **32** (2), 563-572 (1983). DOI: https://doi.org/10.1016/S0007-8506(07)60184-X

[67] E. Soliman, Performance analysis of octal rings as mechanical force transducers. Alex. Eng. J. **54** (2), 155-162 (2015). DOI: https://doi.org/10.1016/j.aej.2015.01.004

[68] C. Sreejith, K.R. Manu Raj, Design and development of a dynamometer for measuring thrust and torque in drilling application. Int. J. Eng. Res. **3** (5), 549-553 (2015). https://iarjset.com/wp-content/uploads/2020/11/Factura-13.pdf

[69] V. Gaikwad, Sharad, M.M. Mahapatra, R.S. Mulik, Design, development, and calibration of octagonal ring type dynamometer with FEA for measurement of drilling thrust and torque. J. Test. Eval. **48** (4), 2699-2712 (2020). DOI: https://doi.org/10.1520/jte20170791

[70] M. Rizal, Husaini, M. Abrar, M.Y. Wiranda, An analytical, numerical and experimental study of an octagonal ring force transducer for a 2-axis force measurement. Int. Semin. Metall. Mater. **541**, 012010 (2019). DOI: https://doi.org/10.1088/1757-899X/541/1/012010

[71] İ. Korkut, A dynamometer design and its construction for milling operation. Mater. Des. **24** (8), 631-637 (2003). DOI: https://doi.org/10.1016/S0261-3069(03)00122-5

[72] S. Karabay, Analysis of drill dynamometer with octagonal ring type transducers for monitoring of cutting forces in drilling and allied process. Mater. Des. **28** (2), 673-685 (2007). DOI: https://doi.org/10.1016/j.matdes.2005.07.008

[73] J. Yao, The CAD of thin extended octagonal ring elastomer. Master's Thesis, Jilin University, Jilin (2005).

[74] H.Z. Guo, Research on octagonal ring strain gauge force measurement experiment based on finite element method. Def. Manuf. Technol. **4**, 65-69 (2016). DOI: https://doi.org/10.3969/j.issn.1674-5574.2016.04.019

[75] H.F. Wang, Study on friction stir joining technology and milling deformation analysis of the joined plate for 7022 aluminum alloy. PhD Thesis, Nanjing University of Aeronautics and Astronautics, Nanjing (2011).